

LASER APPLICATIONS AND OTHER TOPICS IN QUANTUM ELECTRONICS https://doi.org/10.1070/QEL17660

Functional flexible photonics-assisted frequency measurement based on combination of stimulated Brillouin scattering and a Mach–Zehnder interferometer

Lanfeng Huang, Yongjun Li, Shanghong Zhao, Tao Lin, Xuan Li, Guodong Wang, Zihang Zhu

Abstract. **A functional flexible photonics-assisted frequency measurement (PFM) is proposed. Owing to polarisation multiplexing, the electro-optic (O/E) conversion can be performed in a single optical path, which endows the system high stability and concise configuration. Moreover, using a specially designed functional coarse/accurate frequency measurement (C/AFM) module, a large covering range, moderate accuracy, and fast response frequency measurement results can be ensured in a radar warning receiver (RWR), whereas high accurate results can be used in an electronic countermeasures receiver (ECMR). The simulation results show that a strict monotonous amplitude comparison function (ACF) can be constructed based on the structure of a Mach–Zehnder interferometer (MZI) to map the signal frequency, with a measurement error of less than 0.2 GHz in the range of 1–31 GHz. This coarse measurement results can be used to perform radar warning. Based on this result, a highly accurate frequency measurement result is achieved through stimulated Brillouin scattering (SBS). The results reveal that the accuracy is improved to better than 20 MHz. Noteworthy, the C/AFM module consists of purely passive devices, which makes this system meet the potential of integration.**

Keywords: *microwave frequency measurement, microwave photonics, Mach–Zehnder interferometer, stimulated Brillouin scattering.*

1. Introduction

In modern radar warning (RW) and electronic countermeasures (ECM) systems, frequency measurement is an essential task to identify intercepted microwave signals, which is often performed by a specially designed receiver. In an ideal case, it is desirable to possess a wide frequency measurement range, high accuracy and a fast response speed. However, it is very hard to simultaneously satisfy the requirements based on current technology. Therefore, a compromise based on different applications is needed. Usually, a radar warning receiver (RWR) is employed to detect an enemy weapon radar and to provide real-time early warning. In this case, a wide frequency range is required to cover all threats and rapid measurement response, while precious measurement accuracy is not necessary. Differently, an electronic countermeasures receiver (ECMR) is needed to interfere or anti-interfere with specific frequencies, and therefore a higher measurement accuracy is preferred, while the response speed can be relatively low. It should be mentioned that in traditional electronic warfare system, RWRs and ECMRs are two independent sections, which support required frequency measurement results for different applications. However, when considering the requirements of a miniaturised and integrated cognitive detection system in a complicated electromagnetic environment, separate frequency measurement sections would lead to complex structures, serious electromagnetic interference, and high costs. Therefore, an ultracompact reconfigurable frequency measurement system that can provide real-time coarse frequency measurement results for a RWR and accurate frequency information for an ECMR in a wideband range (above 18 GHz) is highly desired. However, for the electrical frequency measurement (EFM), it is hard to satisfy these requirements because of the electronic bottlenecks. Fortunately, microwave photonics technology (MWP) that combines the advantages of electronic and photonic technologies has been proved to be a good method to circumvent the limitations of EFM system.

In recent years, many photonics-assisted frequency measurement (PFM) approaches based on MWP have been reported, whose core principle is to convert the frequency information into another easy-to-observe parameter. These approaches can mainly be divided into several categories, that is, frequency-to-power mapping [1–3], frequency-to-space mapping [4, 5], frequency-to-time mapping [6, 7] and stimulated Brillouin scattering (SBS) [8–13]. The frequency-to-power mapping techniques usually connect the changes in frequency and power through the amplitude comparison function (ACF) established by the characteristics of fibre dispersion elements or filters. However, due to the fundamental tradeoff between the measurement range and accuracy, it can hardly realise wide range and accurate frequency measurement simultaneously. Frequency-to-space mapping and frequency-to-time mapping are two efficient frequency measurement approaches. However, they still face the challenges of instantaneous requirements and concise configuration. As an interesting alternative, the schemes based on SBS have been intensively studied in recent years. The narrow-band filtering obtained by SBS can provide high frequency resolution for photonics-assisted frequency measurement (PFM) applications. In Ref. [12], SBS is utilised to selectively amplify and attenuate sidebands to achieve the conversion from phase modulation (PM) to amplitude modulation (AM), and a measurement range of 9 GHz with a maximum measurement error of 30 MHz is obtained. In Refs [14, 15], the multi-frequency measurement range can be broadened to four times the Brillouin frequency shift by extending the scheme from

Lanfeng Huang, Yongjun Li, Shanghong Zhao, Tao Lin, Xuan Li, Guodong Wang, Zihang Zhu Information and Navigation College, Air Force Engineering University, Xi'an, Shaanxi 710077, China; e-mail: hlf.feng@qq.com

Received 28 July 2021; revision received 22 September 2021
Kvantovaya Elektronika **51** (12) 1135–1143 (2021)
Submitted in English

one pump to two pumps. Additionally, the application of ACF [16] and frequency-phase slope mapping method [17] to further analyse the frequency information in the gain spectrum of SBS can achieve a high precision frequency measurement with the accuracy less than 8 MHz. SBS-based schemes are imperfect, because to identify a proper frequency, they should scan the whole measurement range, resulting in the sacrifice of the measurement response speed. Meanwhile, in these schemes, multiple modulators and multiple optical paths are used in the electro-optic (E/O) conversion sections. It increases the system cost and downgrades the stability. Especially, large modulator array is not easy to be integrated, which will significantly influence the future applications on limited payload platforms such as space-based, air-based, and sea-based ones.

In this paper, a functional flexible PFM scheme based on the combination of stimulated Brillouin scattering and a Mach–Zehnder interferometer (MZI) is proposed and demonstrated. This scheme makes it possible to implement the frequency measurement functions in RWRs and ECMRs through the same configuration. The frequency measurement is carried out in two steps: (*i*) a fast-coarse frequency estimation for the RWR function and (*ii*)an accurate measurement for the ECMR function. Meanwhile, a single polarisation multiplexed modulator is employed to replace the dual optical path and paralleled modulation section, which can simplify the system structure and improve the stability. In addition, the coarse and accurate frequency measurement (C/AFM) module is composed of passive components. It is easily integrable and can provide concise, stable and efficient frequency measurement results for the future compact electronic warfare system.

2. Operation principle and theory

A schematic of the proposed PFM scheme is shown in Fig. 1. The key components of the scheme are a dual-polarisation dual-drive Mach–Zehnder modulator (DPol-DMZM), and a C/AFM module. The modulator is used to simultaneously introduce the unknown RF signal and a frequency sweep signal into the optical domain, while the RWR and ECMR functions are implemented by the C/AFM. The coarse frequency measurement (CFM) for the RWR is performed based on the interference of an MZI, which can instantaneously estimate the unknown RF signal in a wide range. After that, the accurate frequency measurement (AFM) for the ECMR is implemented based on the narrow-band filtering of SBS to improve the measurement accuracy in a narrower range, which makes it possible to shorten the time of scanning and to achieve more accurate frequency information. In this scheme, the DPol-DMZM is an integrated modulator; therefore, the system structure can be simplified and the modulation stability can be improved. Meanwhile, the C/AFM is composed of passive devices and can be integrated into a chip to further simplify the system. The specific operation steps of C/AFM are presented below (where the CFM is implemented from step1 to step3, and the AFM, in the remaining three steps):

1. The unknown RF signal f_x is modulated and sent to the MZI to perform CFM;
2. The optical output power is monitored from the two arms of the MZI.
3. The ACF response is calculated to complete the CFM.
4. The scanning range is determined based on the estimation result of CFM.
5. The optical power is monitored from port 3 of the OC and its mapping with the sweep signal f_s is recorded.
6. The frequency f_s at the power peak and the formula $f_x = f_s + f_B$ are used to calculate f_x in order to complete AFM.

A continuous wavelength laser diode (LD) is used to provide an optical carrier $[E_{in}(t) = E_0 e^{j2\pi f_c(t)}]$ with the amplitude E_0 and frequency f_c. The laser light is sent into the integrated DPol-DMZM modulator, consisting of two parallel DMZMs (DMZM1 and DMZM2), a 3-dB Y branch coupler, a polarisation beam combiner (PBC) and a 90° polarisation rotator

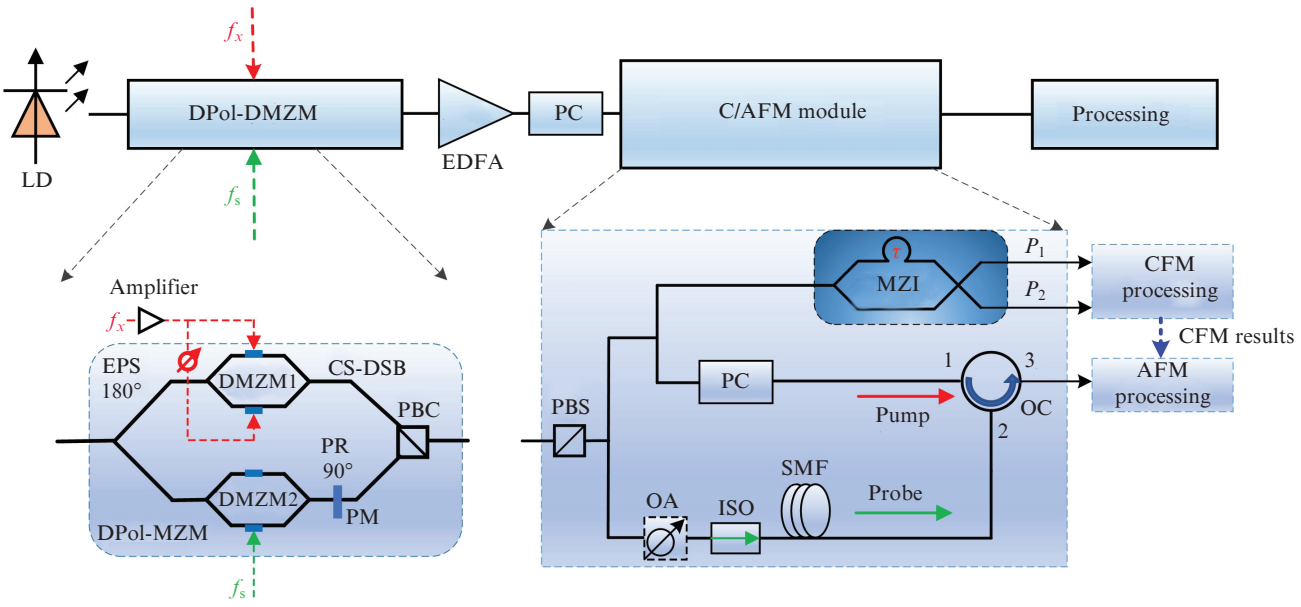

Figure 1. Schematic of the proposed PFM system and the structure of DPol-DMZM: (LD) laser diode; (EPS) electric phase shifter; (PR) polarisation rotator; (PBC) polarisation beam combiner; (EDFA) erbium-doped fibre amplifier; (PBS) polarisation beam splitter; (PC) polarisation controller; (MZI) Mach–Zehnder interferometer; (OA) optical attenuator; (ISO) optical isolator; (SMF) single mode fibre; (OC) optical circulator.

(PR) (see Fig. 1). Due to optical polarisation multiplexing, the DPol-DMZM can simultaneously and separately process the unknown RF signal and frequency sweeping signal in two polarisation states with high isolation. Therefore, it can replace the discrete dual path structure, which is complex and unstable. Here, DMZM1 is biased at the minimum transmission bias point (MITB) of the transfer function. The unknown RF signal is first amplified and then equally divided into two paths. The upper path is directly sent into one RF port of DMZM1, while the lower path is sent into the other RF port after passing through a 180° electric phase shifter (EPS).

Therefore, the carrier-suppressed double sideband (CS-DSB) modulation can be performed. On the other hand, the sweep signal f_s is applied to one RF port of DMZM2, while another port is null. The dc bias voltage of the DMZM2 is set to the quadrature transmission point (QTP) to perform phase modulation. Then the polarisation direction of the DMZM2 output is rotated by the 90° PR. As a result, the modulated signals from DMZM1 and DMZM2 are orthogonally polarised. Finally, these two optical signals are combined by the PBC. To make it more intuitively, we define that the CS-DSB modulated signal from DMZM1 is polarised along the x axis, while the phase modulated signal from DMZM2 is polarised along the y axis.

For convenience, the unknown RF signals can be simply expressed as $V_{RF}(t) = V\sin(2\pi f_x t)$, where V and f_x are the amplitude and frequency of the unknown RF signal. Ignoring the insertion loss of the modulator, the output signal after DMZM1 and DMZM2 can be expressed as

$$E_{DMZM1}(t) = \frac{\sqrt{2}}{2}E_0 J_1(m)\left[e^{j2\pi(f_c - f_x)t} + e^{j2\pi(f_c + f_x)t}\right], \tag{1}$$

$$E_{DMZM2}(t) = \frac{\sqrt{2}}{2}E_0 e^{j2\pi f_c t} \times \left[J_0(m) + J_1(m)e^{j2\pi f_s t} - J_1(m)e^{-j2\pi f_s t}\right], \tag{2}$$

where $J_0(m)$, $J_1(m)$ are the zero- and first-order Bessel function of the first kind; and m is the modulation index. It should be noted that the optical sidebands with orders higher than 2 are ignored because of their low power.

The orthogonally polarised multiplexed signal output from DPol-DMZM is first amplified by EDFA and then sent into the C/AFM module to perform coarse and accurate frequency measurements. Noteworthy, the two optical polarisation states should be firstly controlled to align to the two principal axes of the polarisation beam splitter (PBS) in the module. As is shown in Fig. 1, the optical signal from DPol-DMZM is polarisation de-multiplexed into two paths (x- and y-polarisations) by the PBS. Then, the CS-DSB signal with x-polarisation is further divided into $E_A(t)$ and $E_B(t)$ by an optical power splitter.

2.1. Coarse frequency measurement

After passing a 3-dB power splitter, the optical signal can be expressed as $E_A(t) = E_B(t) = \sqrt{2}/2E_{DMZM1}(t)$. Assuming that the loss of each MZI arm is negligible, the transfer matrixes of the optical signals at two output branches can be written in the form [3]

$$\begin{bmatrix} E_1(t) \\ E_2(t) \end{bmatrix} = \frac{1}{2}\begin{bmatrix} 1 & j \\ j & 1 \end{bmatrix}\begin{bmatrix} e^{j\phi_1} & 0 \\ 0 & e^{j\phi_2} \end{bmatrix}\begin{bmatrix} 1 & j \\ j & 1 \end{bmatrix}\begin{bmatrix} E_A(t) \\ 0 \end{bmatrix} = \frac{1}{2}\begin{bmatrix} E_A(t)e^{j\phi_1} - E_A(t)e^{j\phi_2} \\ jE_A(t)e^{j\phi_1} + jE_A(t)e^{j\phi_2} \end{bmatrix}$$

$$= \frac{1}{2}E_0 J_1(m)\begin{bmatrix} e^{j2\pi(f_c - f_x)t}e^{j\frac{n\pi(f_c - f_x)(L_1 + L_2)}{-c}}\sin(\pi(f_c - f_x)\tau) + e^{j2\pi(f_c + f_x)t}e^{j\frac{n\pi(f_c + f_x)(L_1 + L_2)}{-c}}\sin(\pi(f_c + f_x)\tau) \\ je^{j2\pi(f_c - f_x)t}e^{j\frac{n\pi(f_c - f_x)(L_1 + L_2)}{-c}}\cos(\pi(f_c - f_x)\tau) + je^{j2\pi(f_c + f_x)t}e^{j\frac{n\pi(f_c + f_x)(L_1 + L_2)}{-c}}\cos(\pi(f_c + f_x)\tau) \end{bmatrix}. \tag{3}$$

Here $\Phi_i = -2\pi f_i n L_i/c$ ($i = 1, 2$) is the phase shift induced by the optical paths' lengths (L_1 and L_2) in the two arms of MZI; and n and c are the refractive index and the speed of light in a vacuum, respectively. The time delay τ induced by the path length difference of the MZI is expressed as $\tau = n(L_1 - L_2)/c$. As a result, the optical powers at the two output ports of the MZI can be expressed as

$$P_1 = \frac{1}{4}E_0^2 J_1^2(m)\left\{\sin^2[\pi(f_c - f_x)\tau] + \sin^2[\pi(f_c + f_x)\tau]\right\}$$

$$= \frac{1}{4}E_0^2 J_1^2(m)[1 - \cos(2\pi f_c\tau)\cos(2\pi f_x\tau)],$$

$$P_2 = \frac{1}{4}E_0^2 J_1^2(m)[1 + \cos(2\pi f_c\tau)\cos(2\pi f_x\tau)]. \tag{4}$$

Finally, the amplitude comparison function (ACF) can be constructed as

$$\mathrm{ACF} = \frac{P_1}{P_2} = \frac{1 - \cos(2\pi f_c\tau)\cos(2\pi f_x\tau)}{1 + \cos(2\pi f_c\tau)\cos(2\pi f_x\tau)}. \tag{5}$$

Equation (5) indicates that the value of ACF depends on the optical carrier frequency f_c, the time delay τ, and the unknown RF signal frequency f_x. Since the value of ACF is the ratio of the power of the two branches, the influence of power fluctuation (including RF power and optical power) in this link can be eliminated. Meanwhile, due to the complementary characteristics of the two optical powers of ACF, a monotonic frequency to ACF mapping is $1/2\tau$. It means that in this range, the frequency-ACF look-up table can be established so as to achieve the RF signal frequency by measuring ACF. Additionally, since long fibre is not required, the response speed of the system based on the MZI structure is much faster than that of the schemes utilising an optical fibre dispersion medium. Therefore, the system can provide a fast frequency estimation with moderate accuracy for the RWR.

2.2. Accurate frequency measurement

In fact, ECMR requires accurate frequency measurement results, because the coarse measurement result is not sufficient. To improve the measurement accuracy, the C/AFM module should be functionally switched to AFM. Then, by sweeping f_s we find the exact frequency. It should be emphasised that thanks to the CFM results, the sweeping range can

be greatly compressed. This means we can scan a much narrower band to quickly extract out the fine measurement result. For example, an unknown RF with the frequency of f_x is intercepted by the antenna. Then, the CFM can directly estimate the approximate frequency f_{coarse}. Here, the coarse measurement error is $\Delta_{err} = \pm|f_{coarse} - f_x|$, that is f_x lies in the range of $[f_{coarse} - \Delta_{err}, f_{coarse} + \Delta_{err}]$. Therefore, to scan this range is enough, which may greatly shorten the fine measurement delay.

The CS-DSB signal $E_B(t)$ is selected as the pump light, and its polarisation state is adjusted by the PC to align to the y-polarisation to maximise the intensity of the gain spectrum that is excited by SBS. The phase modulated optical signal with y-polarisation plays the role of the probe signal after passing through the optical attenuator (OA), where the function of the OA is to attenuate the power of the probe light so as to meet the SBS conditions. When the probe signal falls into the pump-induced gain spectrum, the pump power is transferred to the selected sideband, which sharply changes the output optical power from port 3 of the OC. Finally, the mapping relationship between f_s and the output power is collected by the OPM to accurately measure the frequency of the unknown RF signal.

SBS is a nonlinear effect produced by the interaction of two counterpropagating light waves (pump light and Stokes light) via an acoustic wave in the fibre [15]. When the response power threshold of SBS is reached, part of the power of the pump light is transferred to the probe light if a particular frequency matching condition is satisfied, that is, the probe frequency is lower than the pump frequency by a stimulated Brillouin frequency shift ($f_{probe} = f_{pump} - f_B$). Therefore, as shown in Fig. 2, SBS can generate a narrowband gain spectrum around the frequency $f_{pump} - f_B$, which leads to an exponential growth for the probe light, and produce a narrowband loss spectrum at $f_{pump} + f_B$.

In this paper, the two sidebands of the CS-DSB signal are used as the pump light, and the phase modulated signal is selected to be processed by SBS (PM, see Fig. 1). Under small-signal condition, only the optical carrier and the two first-order sidebands are considered. After SBS, the output signal from port 3 of the OC is expressed as

$$E(t) = \frac{\sqrt{2}}{2} E_0 \exp(j2\pi f_c t) \times \begin{Bmatrix} J_0(m) + J_1(m)\exp[g(f_x - f_s - f_B) + \alpha(f_x - f_s + f_B) + j2\pi f_s t] \\ -J_1(m)\exp[g(f_s - f_x - f_B) + \alpha(f_s - f_x + f_B) - j2\pi f_s t] \end{Bmatrix}, \quad (6)$$

where and denote the Brillouin gain and loss respectively, which are defined as [18]

$$g(f) = \frac{g_0 I_p}{2} \frac{(\Delta\nu_B/2)^2}{f^2 + (\Delta\nu_B/2)^2} + j\frac{g_0 I_p}{4} \frac{(\Delta\nu_B/2) f}{f^2 + (\Delta\nu_B/2)^2}, \quad (7)$$

$$\alpha(f) = -g(f) = -\frac{g_0 I_p}{2} \frac{(\Delta\nu_B/2)^2}{f^2 + (\Delta\nu_B/2)^2} - j\frac{g_0 I_p}{4} \frac{(\Delta\nu_B/2) f}{f^2 + (\Delta\nu_B/2)^2}. \quad (8)$$

Here $g(f)$ is the line-centre gain factor; $\Delta\nu_B$ is the Brillouin linewidth; f is the frequency offset to the centre of Brillouin

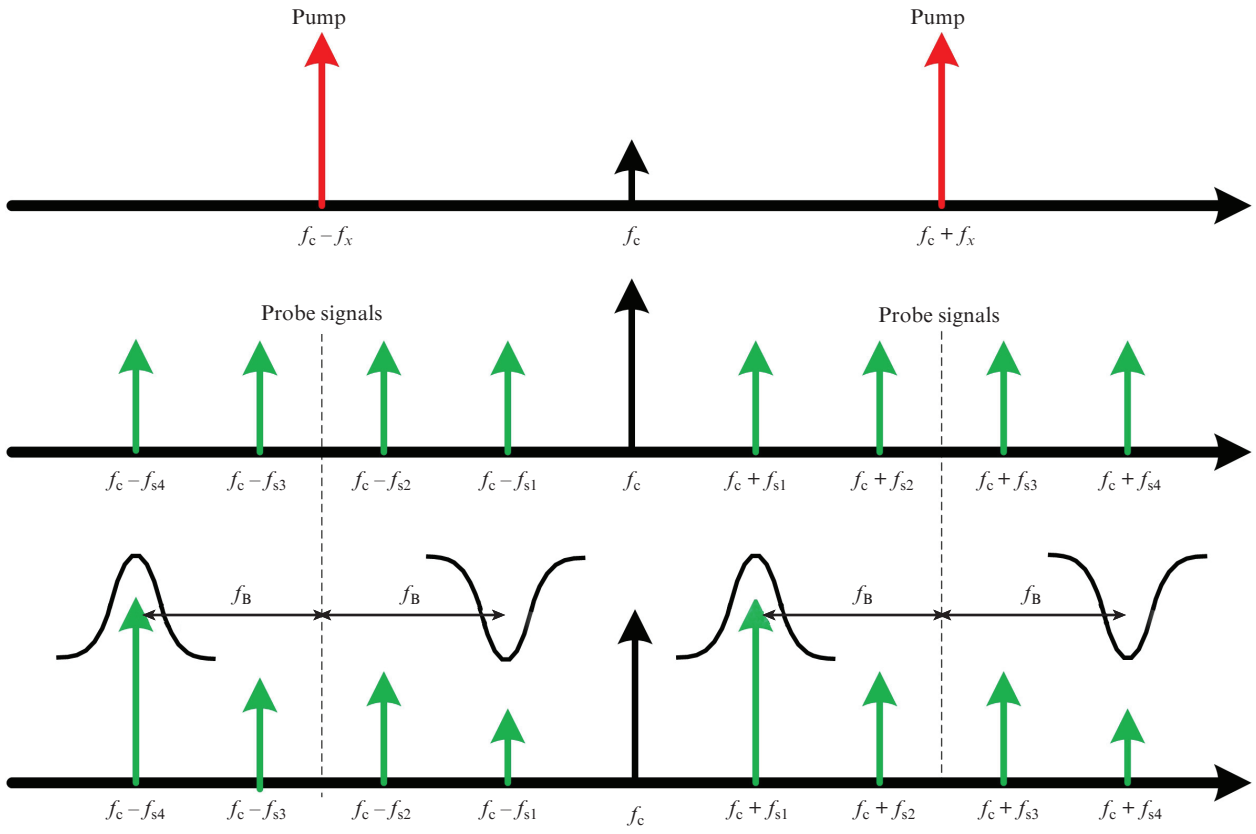

Figure 2. SBS spectrum processing.

linewidth of gain [for $g(f)$] or loss [for $\alpha(f)$)]; and I_p is the pump signal power [16].

Omitting the high order optical sidebands, the optical power entering the OPM can be expressed approximately as

$$P \approx E_0^2 J_0(m) J_1(m) \begin{Bmatrix} G(f_x - f_s - f_B) A(f_x - f_s + f_B) \cos[\phi_g(f_x - f_s - f_B) + \phi_\alpha(f_x - f_s + f_B) + 2\pi f_s t] \\ -G(f_s - f_x - f_B) A(f_s - f_x + f_B) \cos[-\phi_g(f_s - f_x - f_B) - \phi_\alpha(f_s - f_x + f_B) + 2\pi f_s t] \end{Bmatrix}, \quad (9)$$

where, according to Eqns (7) and (8), $G(f) = \exp\{\mathrm{Re}[g(f)]\}$, $A(f) = \exp\{\mathrm{Re}[\alpha(f)]\}$, $\varphi_g(f) = \mathrm{Im}[g(f)]$ and $\varphi_\alpha(f) = \mathrm{Im}[\alpha(f)]$. Therefore, by monitoring the optical power detected by the OPM and recording its mapping relationship with f_s, the unknown RF signal frequency can be accurately determined for EMCR.

3. Simulation demonstration

To verify the proposed PFM approach, the structure shown in Fig. 1 was simulated using the OptiSystem software. The frequency, power and linewidth of the optical carrier emitted from the LD are set to 193.1 THz, 16 dBm and 0.1 MHz, respectively. The half-wavelength voltage of the DPol-DMZM is 4 V, and the extinction ratio is 50 dB. The power of the unknown RF signal is –13 dBm; the gains of the electric amplifier and EDFA are 20 dB and 35 dB, respectively. The time delay τ of the MZI is set to 15 ps, and the length of the SMF is 5 km.

Figure 3 shows the simulation results of the proposed CFM. The measured transmission response from the two output ports of the MZI are shown in Fig. 3a. It can be seen that the two signals have complementary characteristics, which is consistent with the theoretical prediction. The related ACF response and the frequency measurement error between the estimated frequency and the actual input frequency are shown in Fig. 3b. A monotonous interval of ACF, with the maximum frequency measurement range, is near $1/(2\tau)$. Therefore, in this range, the estimated frequency can be obtained from the measured ACF value. As the results show (Fig. 3b), in the range of 1–31 GHz, the measured values of ACF agree well with the theoretical values, and the frequency measurement error between the estimated frequency and the actual input frequency is less than 200 MHz.

According to the above coarse frequency measurement results, we can conclude that the exact frequency may locate in a range, whose centre frequency is the coarsely estimated result (f_{coarse}), and restricted by ±200 MHz. After that, AFM can be performed within this spectral range based on SBS.

In the AFM, the unknown RF signal frequency can be accurately determined by monitoring the optical power of port 3 of the OC. Assuming that the frequency of unknown RF signal is 15 GHz, the mapping relationship between the optical power and the sweep signal f_s is shown in Fig. 4. It can be seen that the narrowband gain spectrum generated by SBS can selectively affect output optical power of port 3 of the OC. Since the probe light is a sweep signal, a frequency can be obtained according to the output peak of the OC when the sweep signal frequency f_s makes the sidebands that stimulated by the unknown signal fall into the gain spectrum of SBS. In this case, the unknown frequency can be calculated by using the formula $f_x = f_s + f_B$. In addition, when the ambient temperature is controlled and the strain of the optical fibre is kept constant, the influence of the surrounding fluctuation on the Brillouin frequency shift f_B can be ignored in the range of 0 GHz–40 GHz [13]. In this simulation, the Brillouin frequency shift is measured at 10 GHz.

The measured results of AFM are shown in Fig. 5a. It can be seen that the measured frequencies are consistent with the input RF frequencies in the frequency range of 1–31 GHz. According to the measurement result and the input frequency, the absolute measurement error and relative measurement error can be obtained. As follows from Fig. 5b, the absolute frequency measurement error is less than 20 MHz, and the

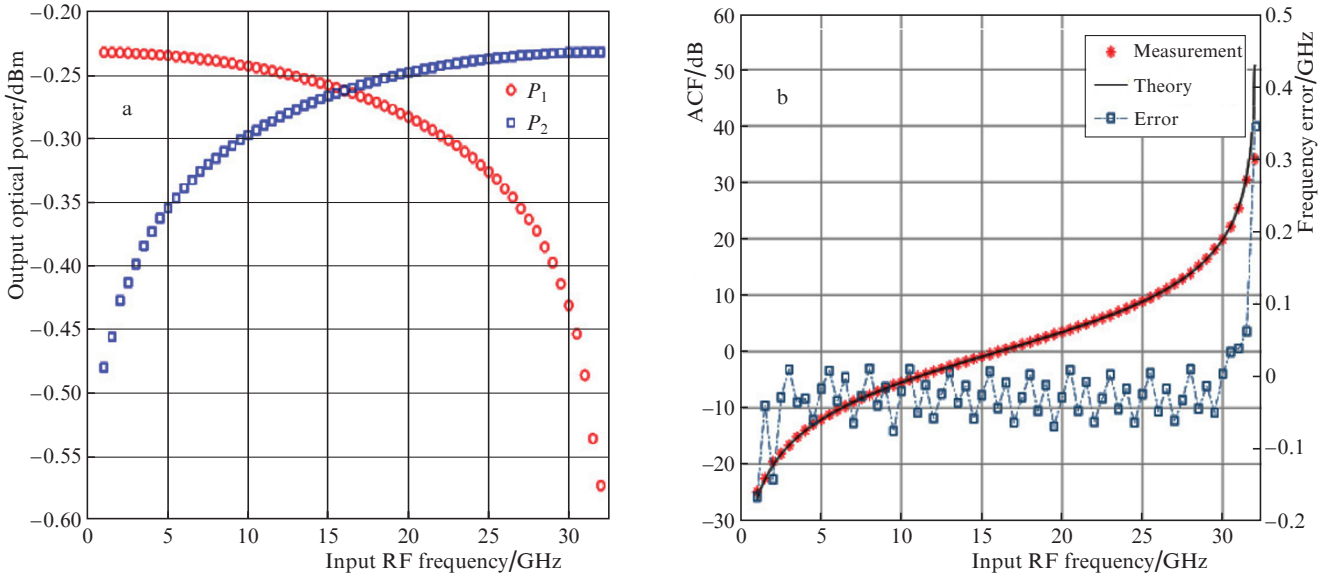

Figure 3. (Colour online) CFM simulation results: (a) measured output optical power at the two output ports of the MZI, and (b) measured ACF and the frequency measurement error between the estimated frequency and the actual input frequency.

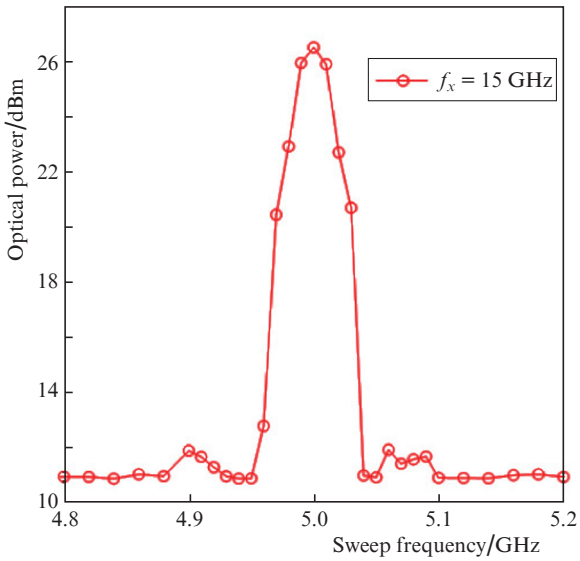

Figure 4. (Colour online) Dependence of the detected optical power on the sweep frequency f_s at f_x = 15 GHz.

relative measurement error is calculated to be less than 1%. Compared to the measurement results from CFM, the accuracy is improved. It should be noted that the AFM accuracy is determined by the SBS gain spectrum. In general, the 3-dB gain bandwidth of SBS is usually about 30 MHz, but when the pump power reaches 15 dBm, the gain bandwidth can be reduced to 10 MHz [19].

4. Analysis and discussion

The simulation revealed that the CFM accuracy is significantly affected by the sideband-to-carrier ratio (SCR) of the CS-DSB signal $E_A(t)$ that injects into MZI. Under ideal conditions, the carrier of $E_A(t)$ is completely suppressed, and the power of the optical signal is mainly concentrated in the first-order sidebands. However, for practical environment, a residual carrier may exist due to the finite extinction ratio of the modulator. Therefore, the SCR of $E_A(t)$ is set between 10 and 25 dB to study the influence of SCR deterioration on the CFM accuracy. The results are shown in Fig. 6. It can be seen that when SCR is sufficiently large (>20 dB), the measurement results agree well with the theoretical analysis. However, when it is too low, the measured results would deviate gradually at high frequencies. The reason is analysed below.

The transmission responses of the two arms (T1 and T2) of MZI are shown in Fig. 7a. The optical carrier is completely suppressed in T2 but reserved in T1, and the first-order sidebands intensity of the CS-DSB signal in T1 is gradually attenuated as f_x increases. Therefore, the influence caused by the optical carrier is mainly from T1. Here, we concentrate on the output result from T1 to investigate how the optical carrier affects the system performance. As can be seen from Fig. 7b, in the case of f_x = 5 GHz, the SCR of the CS-DSB signal in T1 is 14.02 dB; when f_x increases to 31 GHz, the SCR is –12.37 dB. It can be figured out that as f_x increases, the SCR gets lower. The residual carrier occupies the major power of the output signal, which can be hardly ignored. In this case, the symmetrical relationship between T1 and T2 that is shown in Fig. 7a is no longer guaranteed. Therefore, the measured ACF gradually deviates from the theoretical ACF curve in the high frequency range. The power responses of the two output ports of the MZI versus different SCRs are shown in Fig. 7c. It can be seen that the transmission of the T2 branch is almost unchanged. In contrary, the power response of the T1 branch is greatly affected by the SCR. As the SCR increases, the output optical power at the high-frequency range matches better with the theoretical response. Therefore, in practical applications, due to the finite extinction ratio of modulator, it is necessary to connect a fibre Bragg grating (FBG) to exclude the carrier component to ensure well-performed high frequency (>30 GHz) measurement.

Polarisation multiplexing is a significant part of processing in this structure. Therefore, when considering the AFM processing, it is necessary to control the polarisation state to make the optical signals from the two orthogonal polarisa-

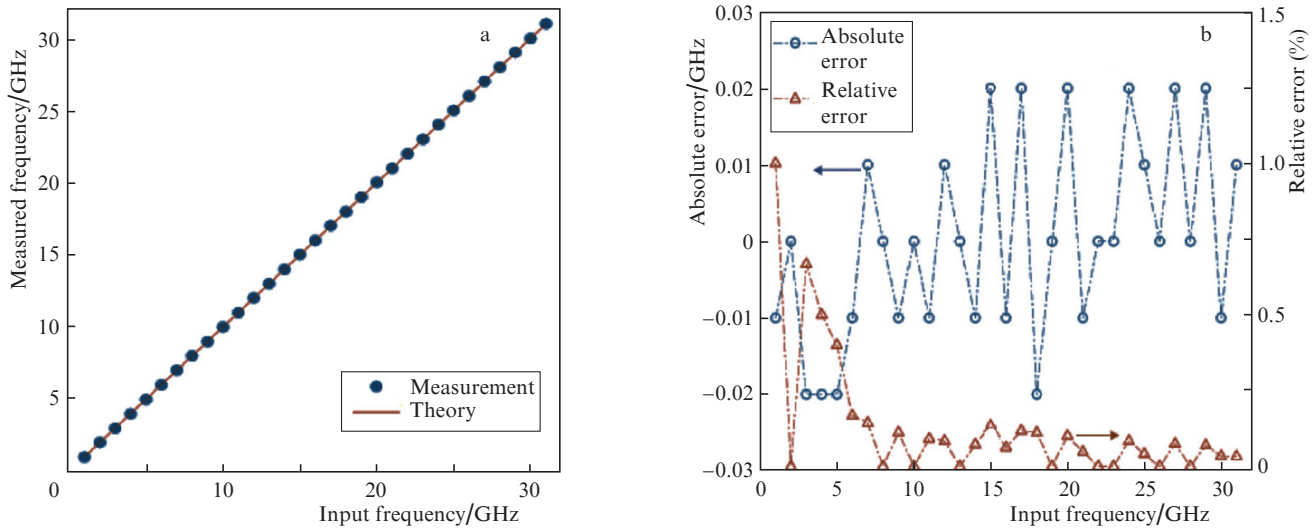

Figure 5. (Colour online) AFM simulation results: (a) dependence of the input frequency on the measured frequency, and (b) dependence of the absolute measurement error and relative error of frequency measurement on the input frequency.

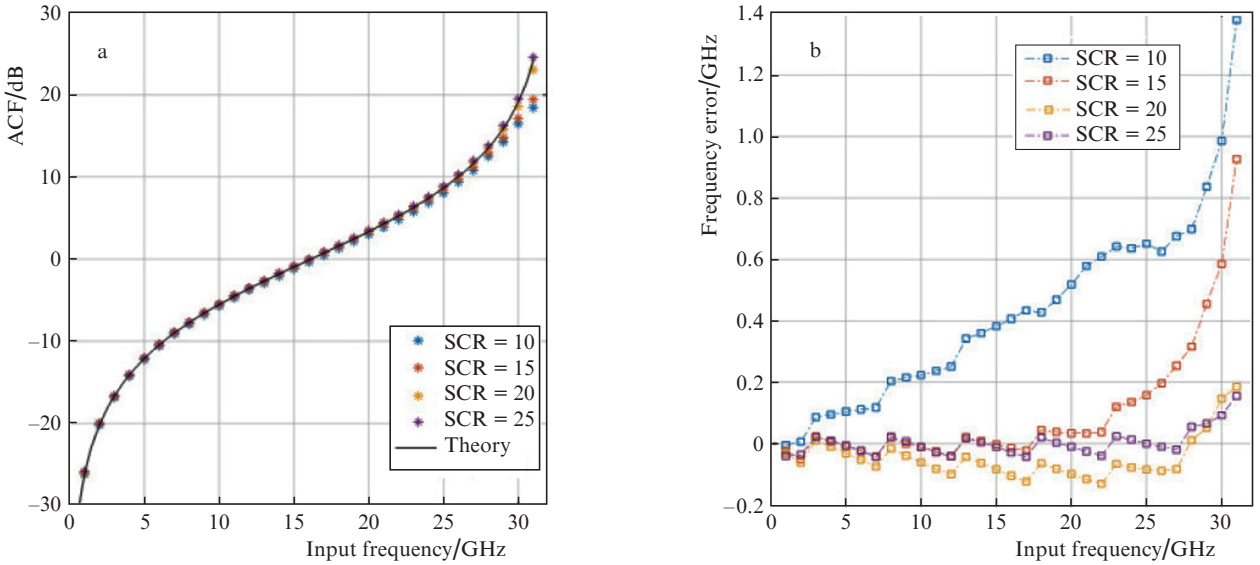

Figure 6. (Colour online) Effect of SCR on CFM accuracy: (a) measured ACF responses of different SCR, and (b) frequency measurement error of different SCR.

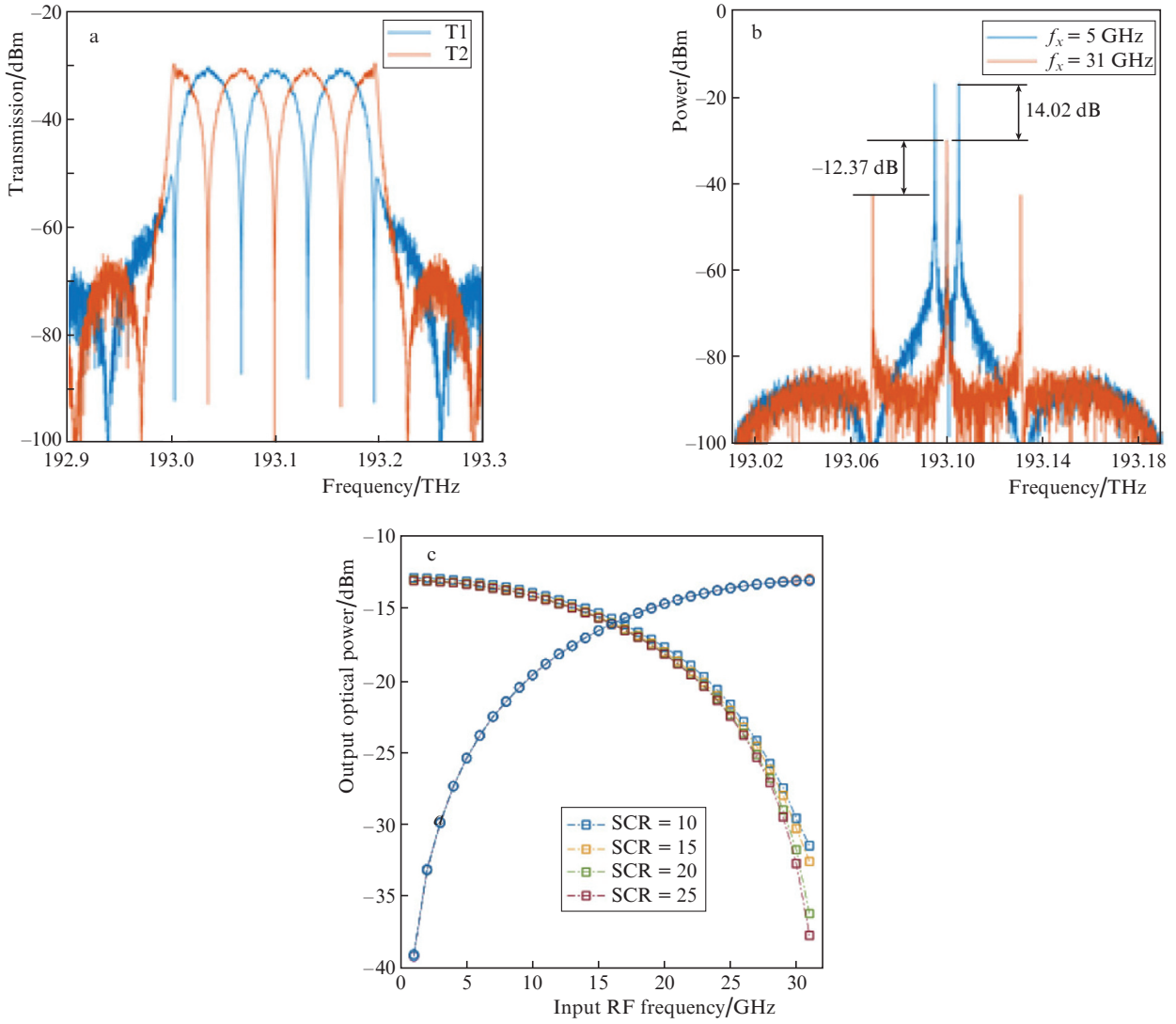

Figure 7. (Colour online) (a) Measured transmission of the two arms of MZI, (b) first-order sidebands intensity and carrier intensity at T1 branch, and (c) output optical power responses of the two arms of MZI vs. different SCRs.

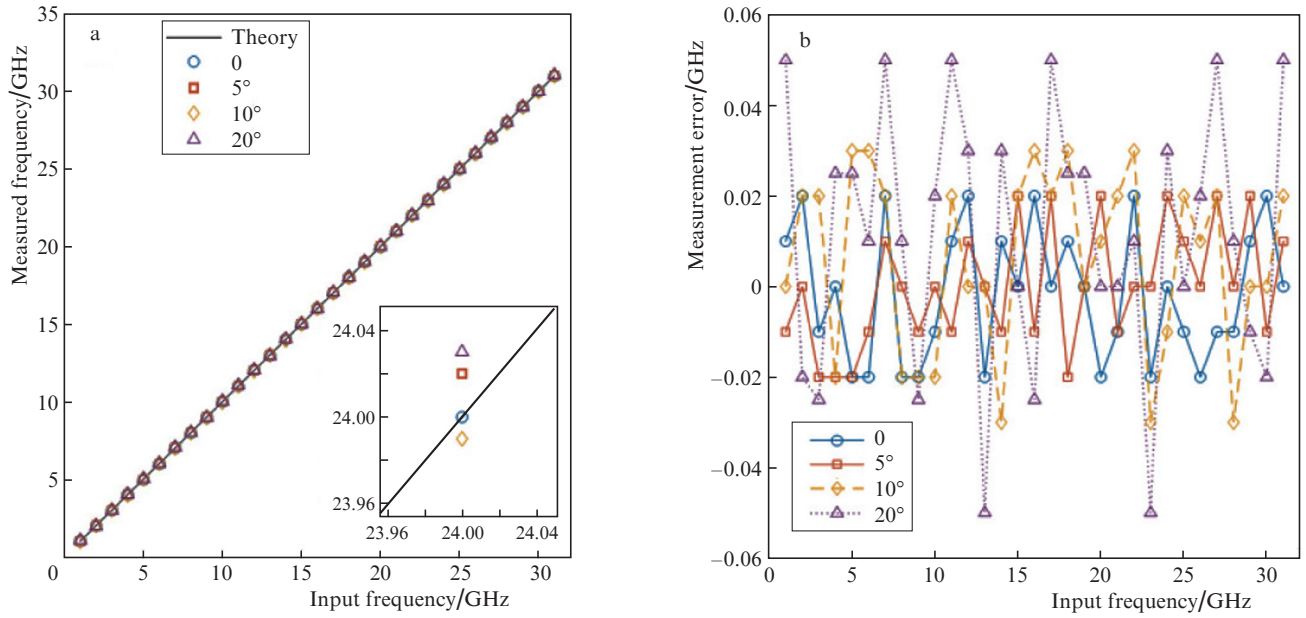

Figure 8. (Colour online) Influence of polarisation deviation on AFM: (a) dependences of the measured frequency on the input frequency, and (b) frequency measurement error at different polarisation deviations.

tions align to each other, so as to maximise the intensity of the gain spectrum excited by SBS. In practical applications, the influence of the environment and the devices will cause polarisation deviation in the system. Therefore, in order to study how the polarisation deviation influences the AFM accuracy, a tiny polarisation disturbance is introduced between $E_B(t)$ and the probe light. The effects of polarisation deviation of the pump light and the probe light on the frequency measurement results are measured when the polarisation deviation varies from 0 to 20°.

As shown in Fig. 8a, when the polarisation deviation is within 10°, the measured frequency is highly consistent with the input RF frequency in the range of 1 – 31 GHz. Moreover, it can be found that the fluctuation range of the frequency measurement result increases with increasing polarisation deviation, which can be seen more clearly in Fig. 8b. When the polarisation deviation is within 5°, the measured maximum error is still less than 20 MHz, the influence on the frequency measurement accuracy can be almost ignored. However, when the polarisation deviation is 10° and 20°, respectively, the maximum measurement error deteriorates to 30 MHz and 50 MHz. Fortunately, when the C/AFM module is integrated into a chip, the polarisation direction can be aligned and fixed before packaging to ensure higher polarisation stability, which can effectively solve the problem of polarisation drift when implemented with discrete devices.

5. Conclusions

A functional flexible PFM scheme based on polarisation multiplexing and coarse/accurate (C/A) compensation is proposed. Under the same system configuration, it can support fast frequency measuring with moderate accuracy and wideband range for the RWR. Moreover, based on the coarse measurement result, the system can perform a more accurate frequency measurement for the ECMR. The frequency measurement for the RWR is performed by MZI-based fast frequency estimation. The determining range can be significantly expanded by utilising strictly monotonous ACF, with a measurement error of less than 0.2 GHz in the range of 1 – 31 GHz. According to the MZI-based coarse frequency measurement result, the related frequency measurement is also implemented for the ECMR. It is realised by the SBS-based accurate frequency measurement. The measurement result reveals that the accuracy is improved to 20 MHz, and the relative error is less than 1 %. Specifically, the E/O modulation section is performed with the assistance of polarisation multiplexing, which improves the stability and simplifies the system. Last but not least, the passive C/AFM module can be integrated into a chip to further simplify the system. The proposed scheme has potential applications in future miniaturised reconnaissance and detection systems.

Acknowledgements. This research was supported in part by the National Natural Science Foundation of China (Grant Nos 61901507 and 62001505) and in part by the Natural Science Foundation of Shaanxi Province (Grant Nos 2019JQ-707 and 2020JQ-469).

References

1. Zhang C., Zhang J., Zhao Z. *Curr. Opt. Photon.*, **4** (4), 361 (2020).
2. Jian D., Xu K., Duan R., et al. *Opt. Commun.*, **284** (24), 5738 (2011).
3. Jian D., Xu K., Sun X., et al. *IEEE Photonics Technol. Lett.*, **22** (15), 1162 (2010).
4. Wiberg A.O.J. et al. *J. Lightwave Technol.*, **32** (20), 3609 (2014).
5. Zou X., Li W., Pan W., Yan L., Yao J. *IEEE Trans. Microwave Theory Tech.*, **61** (9), 3470 (2013).
6. Duan Y., Liao C., Zhou H., et al. *Opt. Express*, **25** (7), 7520 (2017).
7. Nguyen L.V.T. *IEEE Photonics Technol. Lett.*, **21** (10), 642 (2009).
8. Zou X., Xu Sh., Li Sh., et al. *Opt. Lett.*, **44** (23), 5723 (2019).
9. Zhu Z., Merklein M., et al. *Opt. Express,* **27** (9), 12855 (2019).

10. Jiao W., You K., Sun J. *IEEE Photonics J*., **11** (2), 5500912 (2019).
11. Long X., Zou W., Chen J. *Opt. Express*, **25** (3), 2206 (2017).
12. Zheng S., Ge S., Zhang X., Chi H., Jin X. *IEEE Photonics Technol. Lett.*, **24** (13), 1115 (2012).
13. Li W., Zhu N.H., Wang L.X. *Opt. Lett*., **37** (2), 166 (2012).
14. Wu K., Li J., Zhang Y., et al. *Optik*, **126** (19), 1935 (2015).
15. Xiao Y., Guo J., Wu K., et al. *Opt. Express*, **21** (26), 31740 (2013).
16. Wang D., Pan L., Wang Y., et al. *Opt. Laser Technol*., **113** (23), 171 (2019). DOI: 10.1016/j.optlastec.2018.12.035.
17. Wang D., Du C., Yang Y., et al. *Opt. Laser Technol*., **123**, 105895 (2020).
18. Zhang W., Minasian R.A. *IEEE Photonics J*., **4** (5), 1443 (2012).
19. Preussler S., Schneider T. *Opt. Eng*., **55** (3), 031110 (2015).